Two-Dimensional Reverse-Time Migration Applied to GPR With a 3-D-to-2-D Data Conversion

Hai Liu, *Member, IEEE*, Zhijun Long, Bo Tian, Feng Han, Guangyou Fang, and Qing Huo Liu, *Fellow, IEEE*

***Abstract*—Reverse-time migration (RTM) has shown its advantages over other conventional migration algorithms for ground-penetrating radar (GPR) imaging. RTM is preferred to be implemented in the computationally attractive 2-D domain, whereas a real measurement can only be conducted in a 3-D domain. Thus, we propose an asymptotic 3-D-to-2-D data conversion filter in the frequency domain for preprocessing of the recorded data for 2-D RTM. The accuracy of the data conversion filter is verified by two numerical tests on a homogeneous and a layered model. Then, we evaluate the effectiveness of the data conversion filter on the imaging result of 2-D RTM, which is applied to simulated multioffset GPR data from a buried pipe model. With the filter, subsurface image by the 2-D RTM matches better with the 3-D RTM result especially in the aspect of phase congruency. Therefore, we conclude that this data conversion filter is necessary for 2-D RTM. We also conducted a laboratory experiment on a volcanic ash pit using a multiinput–multioutput GPR system, which is adopted on the Chang-E 5 lunar exploration lander and works in a stationary mode. The 3-D-to-2-D data conversion filter is applied to the measured multioffset GPR data before the 2-D RTM. The imaging results demonstrate that three marble slabs buried at different depths up to 2 m are clearly imaged.**

***Index Terms*—Ground-penetrating radar (GPR), lunar exploration, reverse-time migration (RTM), 3-D-to-2-D data conversion.**

I. Introduction

GROUND-PENETRATING radar (GPR) has become a well-recognized geophysical technique for mapping geological structures and detecting buried objects [1]. The applications of GPR are rapidly expanding in various fields, including landmine detection [2], environmental studies [3], civil engineering [4], and lunar exploration [5]. For these GPR applications, accurately imaging the subsurface structure and target is of significant meaning for a correct data interpretation. Due to the similarities between electromagnetic and seismic waves, many migration algorithms developed for seismic imaging [6], e.g., diffraction stacking, Kirchhoff migration, and F-K migration have been successfully implemented to process GPR data. These conventional migration algorithms can greatly enhance the lateral resolution in the reconstructed GPR images through collapsing diffractions and moving dipping reflectors to their true positions. However, these migration methods are based on high-frequency ray approximation or one-way wave propagation, and, thus, can hardly handle a complex velocity model and a steeply dipping reflector.

Reverse-time migration (RTM) has been proved to be of high accuracy in reconstructing an image of complex subsurface structures [7], [8], since it implements the wave propagation inside the media with both forward and backward modeling [9], [10]. The applications of RTM have been extended from seismic imaging to optical imaging [11], as well as GPR imaging [12], [13]. RTM is attractive for true amplitude GPR imaging as it can account for velocity heterogeneity, the radiation pattern [8], topographic variation [14], [15], surface roughness [16], and the effect of losses [17]. Besides, RTM can also easily adopt the prior information of the background media to suppress the clutter [18]. To migrate GPR data, full waveform inversion [18] and travel-time tomography [13] can provide an estimate of the subsurface velocity structure as an initial model for RTM.

Since RTM has to compute the forward and backward wavefields through numerical simulations, it is preferred to implement RTM in the computationally attractive two-dimensional (2-D) domain [12], [15], [19], [20]. The 2-D simulation of wave equation implies an infinite line source extended in the out-of-plane (strike) medium-invariant direction. However, the real measurement of GPR data can only be conducted in a three-dimensional (3-D) domain using an antenna, which can be simplified as a point source in its far field. In a homogenous medium, an electromagnetic point source generates a spherical wavefront, whereas the line-source wavefront is cylindrical [21]. For real GPR acquisition, the radiation pattern is slightly different and depends on the subsurface materials. The amplitude and phase differences associated with the 3-D data acquisition and 2-D modeling can be corrected by full-wave numerical simulations [22], which are, however, computationally expensive. Practically, an asymptotic filter is used to convert the 3-D measured data to its 2-D equivalent [23], [24].

Manuscript received November 1, 2016; revised May 4, 2017 and July 12, 2017; accepted July 21, 2017. Date of publication October 5, 2017; date of current version October 5, 2017. This work was supported in part by the National Natural Science Foundation of China (1504111) and in part by the Scientific Research Foundation for the Returned Overseas Chinese Scholars. *(Corresponding authors: Feng Han and Qing Huo Liu.)*

H. Liu was with the Institute of Electromagnetics and Acoustics, Department of Electronic Science, Xiamen University, Xiamen, 361005, China, and is now with School of Civil Engineering, Guangzhou University, Guangzhou 510006, China (e-mail: liuhai8619@foxmail.com)

Z. Long, B. Tian, and F. Han are with the Institute of Electromagnetics and Acoustics, Department of Electronic Science, Xiamen University, Xiamen, 361005, China (e-mail: feng.han@xmu.edu.cn).

G. Fang is with the Key Laboratory of Electromagnetic Radiation and Sensing Technology, Chinese Academy of Sciences, Beijing 100190, China (e-mail: gyfang@mail.ie.ac.cn).

Q. H. Liu is with the Department of Electrical and Computer Engineering, Duke University, Durham, NC 27708, USA (e-mail: qhl@duke.edu).

Color versions of one or more of the figures in this paper are available online at http://ieeexplore.ieee.org.

Digital Object Identifier 10.1109/JSTARS.2017.2734098

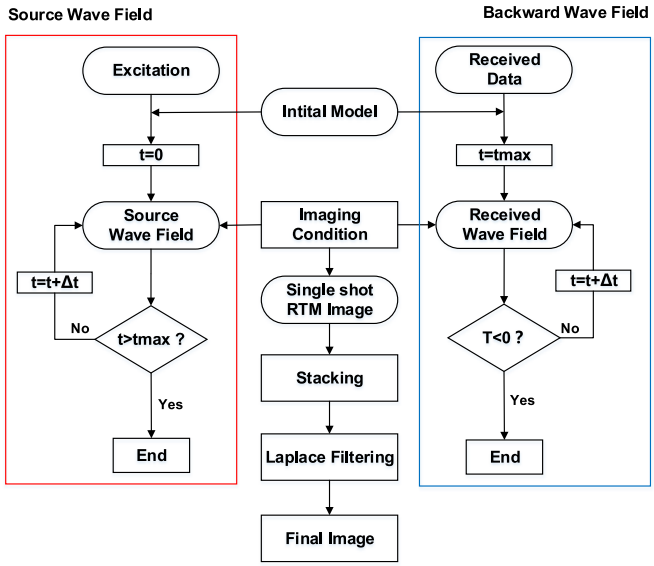

Fig. 1. Flowchart of the 2-D RTM algorithm.

This 3-D-to-2-D data conversion has been adopted for full-waveform inversion of crosshole radar data [25] and provides necessary correction of the 3-D data that is required for recovering conductivity in a 2-D inversion [26]. However, the effectiveness of the data conversion function has been never evaluated for RTM.

In this paper, we evaluate the effectiveness of the 3-D-to-2-D data conversion filter for RTM and apply the 2-D RTM algorithm to converted multioffset GPR data acquired by a multiinput and multioutput (MIMO) GPR system, which is going to be launched for imaging shallow lunar regolith structures. This paper is organized as follows. In Section II, the fundamentals of RTM and the formulations of the 3-D-to-2-D data conversion are introduced. Section III presents numerical experiment results, which demonstrate the effectiveness of the data conversion for RTM of GPR data. In Section IV, we show the RTM results from a laboratory experiment. Section VI provides the discussion and conclusion.

II. Methods

A. Fundamental of RTM

RTM is based on the full-wave equation and can overcome the dip limitation as electromagnetic waves can propagate in any directions. The flowchart of RTM algorithm is illustrated in Fig. 1. The RTM algorithm consists of three primary steps: forward propagation of source wavefield, reverse-time backward propagation of the receiver wavefield, and application of the imaging condition. The same initial model is used for both the forward- and backward-wave propagations. The wavefield extrapolation is implemented in time domain [10] using the finite-difference time-domain (FDTD) method with second-order accuracy in time and fourth-order accuracy in space [27]. In the first step, the electric field over the whole computation domain at each time step during the source propagation is saved in memory. In the second step, the recorded data at all receiver positions are reversed in time and input as boundary conditions for computing the backward wavefield using a negative time step. At each time step of the backward FDTD modeling, the imaging condition is applied for each grid and the correlation between the backward and forward wavefields is integrated over time to yield a reconstructed image of the subsurface for a single transmitter (shot). A Laplacian filter is applied to the stacked image to remove the low-frequency migration artifacts caused by the cross-correlation imaging condition [28].

Various imaging conditions have been proposed for RTM and it is demonstrated that the source-normalized cross-correlation imaging condition can produce the most accurate amplitude reconstruction [29]. Therefore, we adopt it for our RTM algorithm and the expression is given by

$$I(x,z)=\frac{\sum_m \sum_n S_m(n\Delta t,x,z)R_m(n\Delta t,x,z)}{\sum_m \sum_n S_m^2(n\Delta t,x,z)} \quad (1)$$

where $S_m(n\Delta t,x,z)$ is the source wavefield radiated from the mth transmitter at the nth time step, and $R_m(n\Delta t,x,z)$ is the back-propagated wavefield from the recorded data at the receiver locations, and $I(x,z)$ is the reconstructed image from the multioffset GPR data.

B. Three-Dimensional-to-Two-Dimensional Data Conversion

It has been verified that the 2-D and 3-D vector electromagnetic GPR problems can be approximated as scalar acoustic problems [30]. Therefore, we adopt the acoustic transfer function [23] for the 3-D-to-2-D GPR data conversion, which is derived as follows.

The frequency-domain Green's function solution to the wave equation for an omnidirectional point source in a 3-D homogeneous medium is given by

$$G^{3D}(\omega)=\frac{1}{4\pi r}\exp(-jkr) \quad (2)$$

where $k=\omega/v$ is the wavenumber, r is the distance from the source to the observation point, ω is the angular frequency, and v is the propagation velocity of electromagnetic waves. The frequency-domain 2-D Green's function solution for a line source in a full space is given by

$$G^{2D}(\omega)=\frac{-j}{4}H_0^{(2)}(kr) \quad (3)$$

where $H_0^{(2)}$ is the Hankel function of the second kind and zeroth order. Using the large-argument approximation of the Hankel function, which is valid when the distance r is much larger than the wavelength, we obtain

$$G^{2D}(\omega)=\frac{1}{2}\sqrt{\frac{1}{2\pi kr}}\exp(-jkr)\exp\left(-j\frac{\pi}{4}\right). \quad (4)$$

Taking the ratio of the 3-D frequency-domain Green's function in (2) and the asymptotic approximation of the 2-D frequency-domain Green's function in (4), we obtain the asymptotic filter transfer function

$$G^{2D}(\omega)=G^{3D}(\omega)\sqrt{\frac{2\pi\sigma}{|\omega|}}\exp\left(-j\frac{\pi}{4}\right) \quad (5)$$

where σ is defined as $\sigma = vr$. For the general inhomogeneous media in a real word, it is given as the line integral of the velocity with respect to the arc length s of the ray trajectory

$$\sigma = \int v(s)ds. \tag{6}$$

To accurately calculate (5), it is required that reflection events are well separated in time and a velocity model is known beforehand. Thus, a transfer function that is simply based on first arrival time can only be reasonably applicable to the first arrivals of cross-hole radar data [26]. In a real reflection GPR survey, the ray trajectory of a reflection not only depends on the velocity distribution in the subsurface, but also relies on the positions of the transmitter, the receiver, and the reflector. Overlapping arrivals and strongly curved ray paths are commonly observed in a reflection GPR signal. It would be impractical to use (5) for a real reflection GPR. However, the cross-correlation imaging condition given in (1) mainly measures the phase similarity between the source and backward wavefields. Thus, we disregard the amplitude scaling factor σ, and get an asymptotic transfer function, which includes a phase shift and a frequency scaling in the frequency domain. The expression is given by

$$G^{2\mathrm{D}}(\omega) = G^{3\mathrm{D}}(\omega)\frac{1}{\sqrt{|\omega|}}\exp\left(-j\frac{\pi}{4}\right). \tag{7}$$

III. Numerical Experiments

A. Validation of 3-D-to-2-D Data Conversion

In this section, we assess the accuracy of the asymptotic transfer function in (7) for the 3-D-to-2-D data conversion through two numerical experiments, one in a homogeneous medium and the other in a 1-D layered medium. Three-dimensional and 2-D FDTD codes are, respectively, used to compute the radiated wavefield from a point and a line source. To eliminate the impact of the grid dispersion error in the numerical simulation, we use 20 grid points per minimum wavelength (PPW), i.e., PPW equals to 20. In the following numerical experiments, media are assumed to be nonmagnetic, i.e., the relative magnetic permeability equals to 1. We use the first derivative of the Blackman–Harris window (BHW) function [31] with a center frequency of 1 GHz as the exciting source. The accuracy of the asymptotic transfer function is evaluated using the cross-correlation coefficient between the 2-D simulated data and the converted 3-D simulated data

$$R = \frac{\sum_n x_{2\mathrm{D}} x_{3\mathrm{D}}}{\sqrt{\sum_n {x_{2\mathrm{D}}}^2 \sum_n {x_{3\mathrm{D}}}^2}} \tag{8}$$

where $x_{2\mathrm{D}}$ is the simulated 2-D GPR trace, $x_{3\mathrm{D}}$ is the converted 3-D GPR trace, and n is the time sample. For comparison, we also calculated the cross-correlation coefficient between the 2-D data and the original 3-D data.

First, we test the data conversion filter for the simplest case, a homogeneous medium with relative permittivity and conductivity equal to 3 and 0.1 mS/m, respectively. The comparison among the 2-D, 3-D, and converted 3-D electric fields is shown in Fig. 2. For better observation of the phase differences, we show the data after normalization in Fig. 2(b). We can see that a distinct phase difference exists between the 3-D and 2-D wavelets and their cross-correlation coefficient is calculated to be 0.776. After the 3-D-to-2-D data conversion, we can hardly discern the difference between the converted 3-D and 2-D data, and their cross-correlation coefficient reaches 0.998.

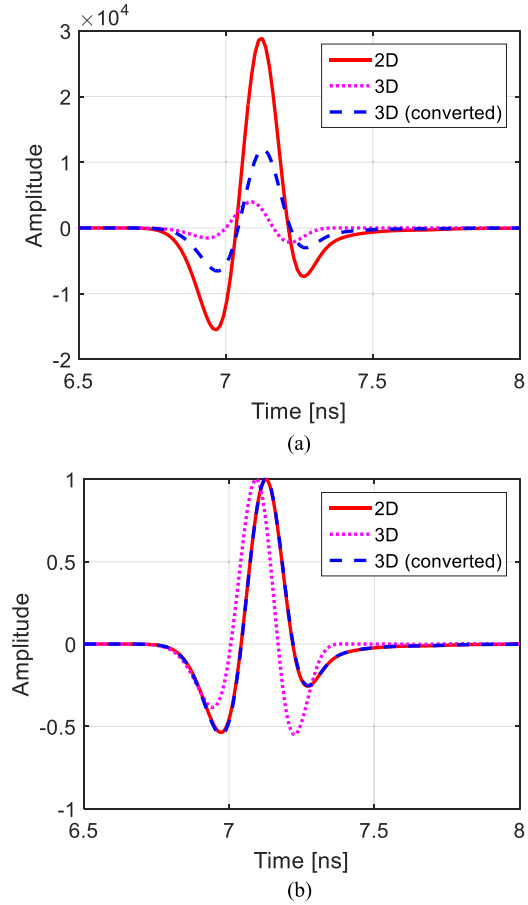

Fig. 2. Comparison among the 2-D, 3-D, and converted 3-D electric fields propagating in a homogeneous full space. The 2-D and 3-D waveforms are recorded by a simulating receiver at 1.5 m away from a source. (a) Original data and (b) data after normalization.

The second numerical test is conducted on a 1-D layered model, as shown in Fig. 3(a). Fig. 3(b) shows the simulated data after normalization. We can readily identify the direct air wave, surface reflection, and the reflection from the subsurface interface, which arrive at 5, 8, and 11 ns, respectively. We can observe that a distinct phase difference exists between the simulated 3-D and 2-D data. The strong direct wave is considered as a noise in migration, so the quality of data conversion is evaluated using the weak reflections, which are useful signals [13]. The cross-correlation coefficient of the reflection signals in the simulated 3-D and 2-D data is calculated to be 0.732. After the 3-D-to-2-D data conversion, the converted 3-D data matches well with the 2-D data, and their cross-correlation coefficient reaches 0.996.

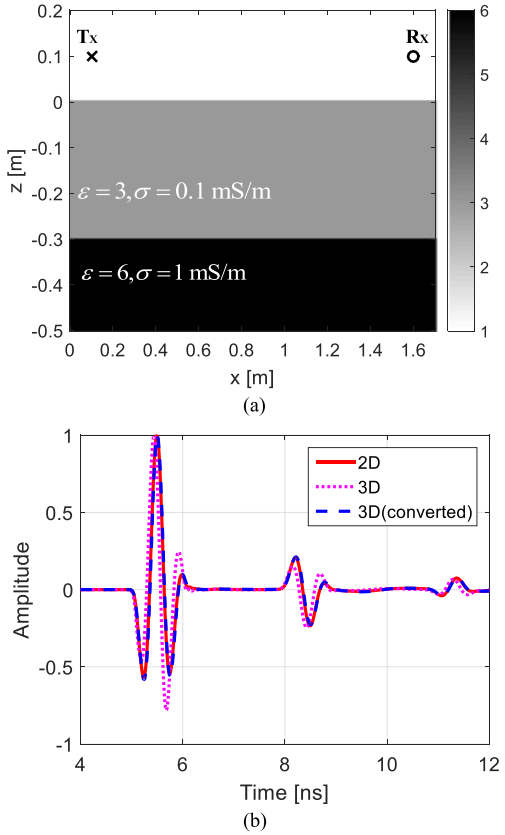

Fig. 3. Comparison among the 2-D, 3-D, and converted 3-D electric fields propagating in a layered model. The 2-D and 3-D waveforms are recorded by a simulating receiver at 1.5 m away from a source, both lying 0.1 m above the air/ground interface. (a) Simulation model and (b) simulated data after normalization.

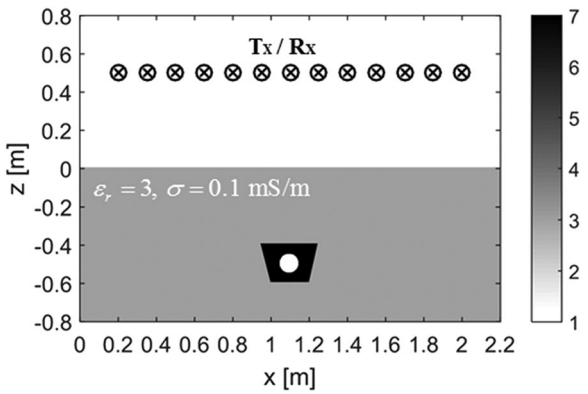

Fig. 4. Buried pipe model for evaluating the 2-D RTM algorithm. The source and receiver positions are, respectively, indicated by a cross and a circle. An air-filled concrete (electric conductivity equals to 1 mS/m) pipe is buried at a depth of 0.4 m.

B. Two-Dimensional RTM Imaging

In this section, we use a buried pipe model (shown in Fig. 4) to validate the 2-D RTM algorithm and the effectiveness of the 3-D-to-2-D data conversion filter on the imaging results. Three-dimensional FDTD code is used to compute the radiated wavefield from a point and simulated 3-D data are used

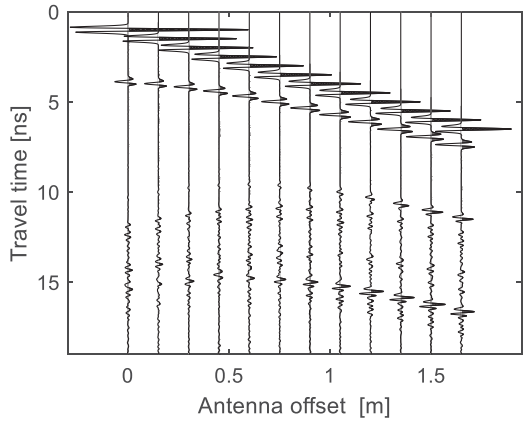

Fig. 5. Example of the simulated common-source GPR profile from the model in Fig. 4. Time-variant gain has been applied for better presentation of the reflected signal from the buried object.

for the following RTM. The 3-D model was set up by extending the 2-D model in Fig. 4 in the third direction (y-direction). PPW was set to be 15 and we use a BHW source with a center frequency of 2 GHz. Fig. 5 shows an example of the simulated common-source GPR profiles. To evaluate the effectiveness of the 3-D-to-2-D conversion filter on the 2-D RTM, we first reconstruct the subsurface image by 3-D RTM using the simulated 3-D data and use it as the ground truth. Then, we reconstruct the images by 2-D RTM using the simulated 3-D data and the converted 3-D data. Since the velocity structure in the subsurface is usually unknown in real measurement, we use a constant-velocity half-space model for the RTM. The migrated images are shown in Fig. 6. We can observe the distinct phase difference between Fig. 6(a) and (b). However, the difference between Fig. 6(a) and (c) can be hardly distinguished. To investigate influence of the noise, which is unavoidable in real measurement, on the proposed imaging procedure, we added the white noise to the simulated GPR dataset. The signal-to-noise ratio (SNR) is set to be 10 dB. The reconstructed subsurface images are shown in Fig. 6(e)–(g). More clutter can be observed, compared with the noise-free results in Fig. 6(a)–(c). Nevertheless, Fig. 6(g) matches better with Fig. 6(e) than Fig. 6(f). This means that the 3-D-to-2-D data conversion is effective for the 2-D RTM.

To better demonstrate the effectiveness of the 3-D-to-2-D data conversion filter on 2-D RTM, we compare two sample traces from the RTM results at position of 1.1 m (center of the pipe) and 1.2 m (edge of the pipe). The results are shown in Fig. 7. For the noise-free results in Fig. 7(a) and (b), the cross-correlation coefficient increases from 0.921 (between the solid and dashed curves) to 0.955 (between the solid and dotted curves) at the first position, and increases from 0.923 to 0.957 at the second position. For the noisy results in Fig. 7(c) and (d), the cross-correlation coefficient increases from 0.903 (between the solid and dashed curves) to 0.934 (between the solid and dotted curves) at the first position, and increases from 0.884 to 0.922 at the second position. Although the influence of the noise makes the overall match between the 3-D RTM and 2-D RTM results

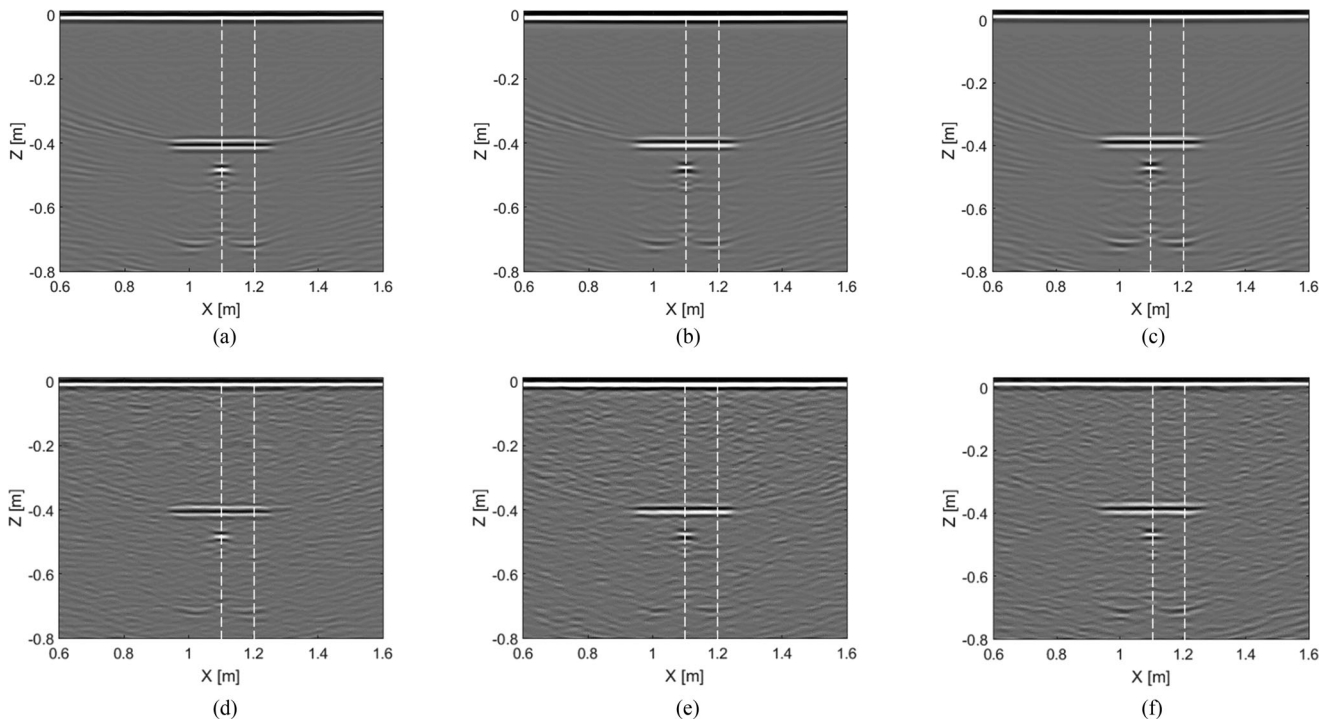

Fig. 6. Reconstructed subsurface images of the concrete pipe model in Fig. 4 by (a), (d) 3-D RTM using the simulated 3-D dataset, (b), (e) 2-D RTM using the simulated 3-D dataset, and (c), (f) 2-D RTM using the converted 3-D dataset without (up) and with (bottom) noise.

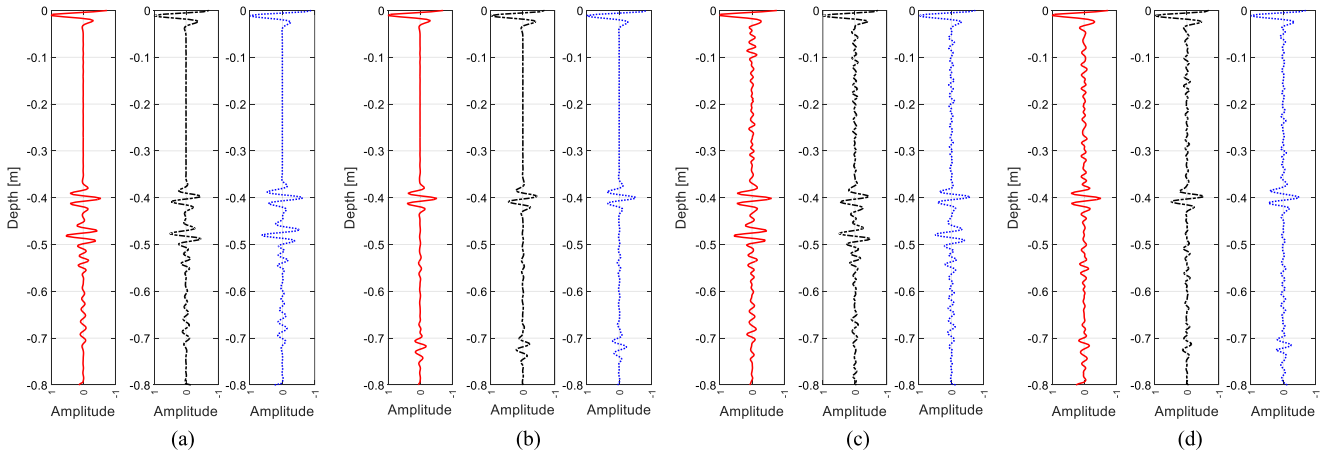

Fig. 7. Comparison of sample traces from the RTM results in Fig. 6 at (a), (c) $x = 1.1$ m and (b), (d) $x = 1.2$ m. (a), (b) are extracted from the noise-free results in Fig. 6 (a)–(c), while (c), (d) are from the noisy results in Fig. 6(e)–(g). The solid, dashed, and dotted curves from the left to right in each panel are produced by 3-D RTM using the simulated 3-D dataset, 2-D RTM using the simulated 2-D dataset, and 2-D RTM using the converted 3-D dataset, respectively. Better match between the soild and dotted curves than that between the solid and dashed curves can be easily observed no matter the noise (SNR = 10 dB) is added or not.

decreased, it is evident that the 3-D-to-2-D data conversion can yield more close (accurate) image to the 3-D RTM, especially in the aspect of the phase congruency. Therefore, we conclude that the asymptotic 3-D-to-2-D data conversion filter does work for GPR, although it is based on the far-field assumption.

IV. Laboratory Experiment

A MIMO GPR system is going to be launched to the moon by the China's Chang-E 5 lunar exploration mission in 2017. Fig. 8 shows a schematic drawing of the Change-E 5 lander [32]. This lander is equipped with an impulse GPR system and 12 off-ground Vivaldi antennas, one of which is sequentially used as a transmitter and the other 11 receive the radar echoes at a height of about 90 cm above the lunar surface. The layout of the 12 antennas is presented in [33]. Since two of the 12 antennas are out of the 2-D imaging plane containing the driller, we use only ten Vivaldi antennas for the 2-D RTM, but unlike a usual GPR system, this MIMO GPR system is fixed at a

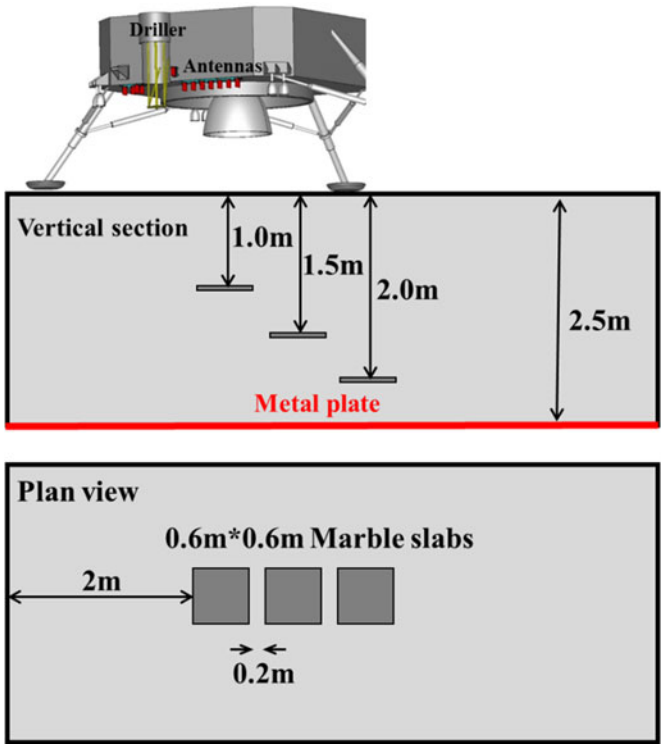

Fig. 8. Schematic diagram of the laboratory experiment on a volcanic ash pit using the MIMO GPR system, which is equipped on a real-size model of the Chang-E 5 lander to be launched to the moon in 2017. Three marble slabs were sequentially buried at different depths in the volcanic ash. The measurement was repeated at three positions to image the three marble slabs, respectively.

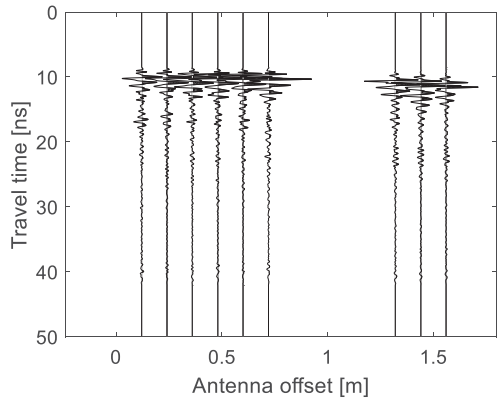

Fig. 9. Example of the measured common-source GPR profile when the lander was place over the marble buried at 0.5-m depth.

position and works in a stationary mode. We have to image the lunar regolith structure and the distribution of lunar rocks below the driller (indicated in Fig. 8) from the total 90 GPR traces. In this section, we show the results of 2-D RTM applied to the laboratory experimental data.

In the laboratory, a 7 m $\times$ 3 m $\times$ 2.5 m pit filled with volcanic ash is used to simulate the lunar soil. The relative dielectric permittivity of the volcanic ash is about 2.5 and its electric conductivity is negligibly small. We buried three marble slabs at depths of 1, 1.5, and 2 m, respectively, in the volcanic ash pit, as shown in Fig. 8. The thickness and relative dielectric permittivity of the marble slab are 3 cm and about 8, respectively. At a depth of 2.5 m, i.e., at the bottom of the ash pit, there is a metal plate. A real-size model of the Chang-E 5 lander equipped with the MIMO GPR system was place on the ground to detect the subsurface targets, and 90 GPR traces were recorded. Due to the limited aperture of the antenna array, the measurement was repeated at three horizontal positions to image the three marble slabs, which was sequentially buried. The source wavelets radiated from each transmitting antenna were recorded as input of the RTM algorithm by lifting the lander at a height of about 4 m from the ground. The center frequency of the source impulse is around 2 GHz and the effective frequency band is from 1 to 3 GHz.

The procedure for preprocessing the GPR traces consists of a constant gain, dc removal, dewow, cable delay correction, background removal, and the 3-D-to-2-D data conversion. A time-variant gain has been applied in the receiver of the GPR system to compensate energy loss mainly due to the wavefront spreading. The cable delay correction compensates the time delays through the coaxial cable and from the antenna feeding point to the antenna phase center [34]. After the correction, the Vivaldi antenna is simplified as a point source. The background removal is conducted to eliminate the strong antenna coupling, interfering reflection signal from the lander and other clutters. The background signal is measured by lifting the lander at a height of 4 m from the ground surface and subtracted from the measured signal in the aforementioned laboratory experiment. Through this background removal, we can suppress the antenna coupling and reflection from the lander, rather than the antenna–ground interactions. Fig. 9 shows an example of the measured common-source GPR profile after data processing. The 3-D-to-2-D data conversion is implemented using the asymptotic filtering given by (7) in the frequency domain, which add a little computing cost compared to the RTM. After the data preprocessing, a tapered time window is applied to exclude the interfering reflection from the reinforced concrete walls of the ash pit, a nearby metal window of the laboratory room, etc. The parameters of such time window are designed according to the known depths of the targets.

A half-space model, in which the relative dielectric permittivity and electric conductivity of the volcanic ash are set to be 2.5 and 0.1 mS/m, is used as the initial model for the 2-D RTM. A Laplacian filter is applied to the RTM results of the three marble to remove the low-frequency migration artifacts caused by the source-normalized cross-correlation imaging condition. Fig. 10 shows the reconstructed images of the three marble slabs. The ground surface and the buried marbles at different depths are clearly imaged. The images of the three marble slabs are in good consistence with their true locations. However, we can see that the horizontal resolution is poor and some artifacts exist besides the marble events. The horizontal resolution is constrained by the limited aperture of the antenna array used by the fixed MIMO GPR system, which consists of only ten antennas and records 90 GPR traces.

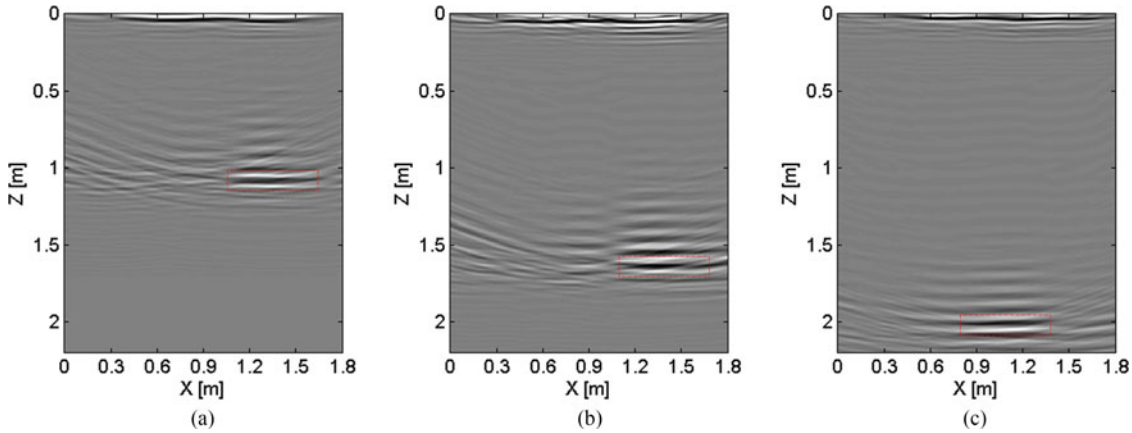

Fig. 10. Imaging results of 2-D RTM applied to the three MIMO GPR datasets acquired in laboratory. (a) 1-m marble; (b) 1.5-m marble; and (c) 2-m marble. The true location of the marbles is indicated by dotted boxes.

V. Conclusion

In this paper, we quantitatively evaluated the accuracy of an asymptotic 3-D-to-2-D data conversion filter for processing GPR data, as well as the effectiveness of the conversion filter on the 2-D RTM. The accuracy of the data conversion filter is verified by two numerical tests on a homogeneous and a layered model. The distinct phase difference between the simulated 3-D and 2-D data can be effectively corrected by the conversion filter. The cross-correlation coefficient between the converted 3-D data and the 2-D data increases from 0.965 to 0.994. The effectiveness of the data conversion filter on the imaging result of the 2-D RTM is evaluated using simulated multioffset GPR data from a buried pipe model. With the filter, subsurface image by the 2-D RTM matches better with the 3-D RTM result, and we conclude that this data conversion filter is necessary for the 2-D RTM, especially in the aspect of phase congruency. Therefore, we conclude that this 3-D-to-2-D data conversion filter is necessary for 2-D RTM.

We also conducted a laboratory experiment on a volcanic ash pit using a MIMO GPR system, which is equipped to the Chang-E 5 lunar exploration lander and works in a stationary mode. The 3-D-to-2-D data conversion filter is applied to the measured multioffset GPR data before the 2-D RTM. The imaging results demonstrate that three marble slabs buried at different depths up to 2 m are clearly imaged, and, thus, verified that the mission for imaging the lunar regolith structure and the distribution of lunar rocks of the Chang-E 5 lunar exploration lander can be successfully fulfilled.

References

[1] H. M. Jol, *Ground Penetrating Radar Theory and Applications*. Amsterdam, The Netherlands: Elsevier, 2009, pp. 4–6.

[2] X. Feng and M. Sato, "Pre-stack migration applied to GPR for landmine detection," *Inverse Probl.*, vol. 20, no. 6, pp. S99–S115, 2004.

[3] H. Liu, K. Takahashi, and M. Sato, "Measurement of dielectric permittivity and thickness of snow and ice on a brackish lagoon using GPR," *IEEE J. Sel. Topics Appl. Earth Obs. Remote Sens.*, vol. 7, no. 3, pp. 820–827, Mar. 2014.

[4] H. Liu and M. Sato, "In situ measurement of pavement thickness and dielectric permittivity by GPR using an antenna array," *NDT E Int.*, vol. 64, pp. 65–71, Jun. 2014.

[5] L. Xiao *et al.*, "A young multilayered terrane of the northern mare imbrium revealed by Chang'E-3 mission," *Science*, vol. 347, no. 6227, pp. 1226–1229, Mar. 2015.

[6] O. Yilmaz, *Seismic Data Analysis*. Tulsa, OK, USA: Society of Exploration Geophysicists, 2001.

[7] J. Zhu and L. R. Lines, "Comparing of Kirchhoff and reverse-time migration methods with application to prestack depth imaging of complex structures," *Geophysics*, vol. 63, no. 4, pp. 1166–1176, 1998.

[8] J. H. Bradford, J. Rozar, D. Wilkins, and R. Ford, "Reverse time migration from rugged topography to image ground-penetrating radar data in complex environments," in *Proc. 7th Int. Conf. Environ. Eng. Geophys.*, 2016, pp. 115–118.

[9] W.-F. Chang and G. A. McMechan, "Reverse-time migration of offset vertical seismic profiling data using the excitation-time imaging condition," *Geophysics*, vol. 51, no. 1, pp. 67–84, 1986.

[10] E. Baysal, D. D. Kosloffs, and J. W. C. Sherwood, "Reverse time migration," *Geophysics*, vol. 48, no. 11, pp. 1514–1524, 1983.

[11] Z. Wang, H. Ding, G. Lu, and X. Bi, "Reverse-time migration based optical imaging reverse," *IEEE Trans. Med. Imag.*, vol. 35, no. 1, pp. 273–281, Jan. 2016.

[12] E. Fisher, "Examples of reverse-time migration of single-channel, ground-penetrating radar profiles," *Geophysics*, vol. 57, no. 4, pp. 577–586, 1992.

[13] H. Zhou and M. Sato, "Subsurface cavity imaging by crosshole borehole radar measurements," *IEEE Trans. Geosci. Remote Sens.*, vol. 42, no. 2, pp. 335–341, Feb. 2004.

[14] W. Zhu, Q. Huang, and L. Liu, "Application of reverse time migration on GPR data for detecting internal structures in a sand dune," in *Proc. 2015 SEG Annu. Meet. Tech. Program Expanded Abstracts*, 2015, pp. 2269–2274.

[15] J. H. Bradford, "Reverse-time prestack depth migration of GPR data from topography for amplitude reconstruction in complex environments," *J. Earth Sci.*, vol. 26, no. 6, pp. 791–798, 2015.

[16] L. Fu, S. Liu, L. Liu, and J. Wu, "Airborne ground penetrating radar numerical simulation and reverse time migration," *Chin. J. Geophys.*, vol. 57, no. 5, pp. 1636–1646, 2014.

[17] T. Zhu, J. M. Carcione, and M. A. B. Botelho, "Reverse time imaging of ground-penetrating radar and SH-seismic data including the effects of wave loss," *Geophysics*, vol. 81, no. 4, pp. H21–H32, 2016.

[18] H. Yang, T. Li, N. Li, Z. He, and Q. H. Liu, "Time-gating-based time reversal imaging for impulse borehole radar in layered media," *IEEE Trans. Geosci. Remote Sens.*, vol. 54, no. 5, pp. 2695–2705, May 2016.

[19] S. Liu, L. Lei, L. Fu, and J. Wu, "Application of pre-stack reverse time migration based on FWI velocity estimation to ground penetrating radar data," *J. Appl. Geophys.*, vol. 107, pp. 1–7, 2014.

[20] C. J. Leuschen and R. G. Plumb, "A matched-filter-based reverse-time migration algorithm for ground-penetrating radar data," *IEEE Trans. Geosci. Remote Sens.*, vol. 39, no. 5, pp. 929–936, May 2001.

[21] L. Auer, A. M. Nuber, S. A. Greenhalgh, H. Maurer, and S. Marelli, "A critical appraisal of asymptotic 3D-to-2D data transformation in full-waveform seismic crosshole tomography," *Geophysics*, vol. 78, no. 6, pp. R235–R247, 2013.

[22] H. Zhou, M. Sato, S. Member, T. Takenaka, and G. Li, "Reconstruction from antenna-transformed radar data using a time-domain reconstruction method," *IEEE Trans. Geosci. Remote Sens.*, vol. 45, no. 3, pp. 689–696, Mar. 2007.
[23] N. Bleistien, "Two and one half dimensional in plane wave propagation," *Geophys. Prospecting*, vol. 34, no. 5, pp. 686–703, 1986.
[24] M. Yedlin, D. Van Vorst, and J. Virieux, "Uniform asymptotic conversion of Helmholtz data from 3D to 2D," *J. Appl. Geophys.*, vol. 78, pp. 2–8, 2012.
[25] J. R. Ernst, A. G. Green, H. Maurer, and K. Holliger, "Application of a new 2D time-domain full-waveform inversion scheme to crosshole radar data," *Geophysics*, vol. 72, no. 5, pp. J53—J64, 2007.
[26] D. G. Van Vorst, M. J. Yedlin, J. Virieux, and E. S. Krebes, "Three-dimensional to two-dimensional data conversion for electromagnetic wave propagation using an acoustic transfer function: Application to cross-hole GPR data," *Geophys. J. Int.*, vol. 198, no. 1, pp. 474–483, 2014.
[27] J. Irving and R. Knight, "Numerical modeling of ground-penetrating radar in 2-D using MATLAB," *Comput. Geosci.*, vol. 32, no. 9, pp. 1247–1258, 2006.
[28] Y. Zhang and J. Sun, "Practical issues in reverse time migration: True amplitude gathers, noise removal and harmonic source encoding," *First Break*, vol. 26, pp. 29–35, Jan. 2009.
[29] S. Chattopadhyay and G. A. McMechan, "Imaging conditions for prestack reverse-time migration," *Geophysics*, vol. 73, no. 3, pp. S81–S89, 2008.
[30] D. Van Vorst, "Cross-hole GPR imaging: Traveltime and frequency-domain full-waveform inversion," Ph.D. dissertation, Dept. Electr. Comput. Eng., Univ. British Columbia, Vancouver, BC, Canada, Dec. 2015.
[31] Y. H. Chen, W. C. Chew, and M. L. Oristaglio, "Application of perfectly matched layers to the transient modeling of subsurface EM problems," *Geophysics*, vol. 62, no. 6, pp. 1730–1736, 1997.
[32] Y. X. Li, G. Y. Fang, Y. C. Ji, B. Zhou, and S. X. Shen, "Data processing and some results of Chang'E-5 LRPR ground verification," in *Proc. 2016 16th Int. Conf. Ground Penetrating Radar*, 2016, pp. 1–4.
[33] W. L. Ji, Y. C. B. Zhou, and Y. G. Fang, "Design of an array antenna system for Chang'E-5 LRPR," in *Proc. 2016 16th Int. Conf. Ground Penetrating Radar*, 2016, pp. 1–4.
[34] H. Liu and M. Sato, "Determination of the phase center position and delay of a Vivaldi antenna," *IEICE Electron. Exp.*, vol. 10, no. 21, pp. 1–7, 2013.

Hai Liu (S'11–M'13) received the B.E. and M.E. degrees in civil engineering from Tongji University, Shanghai, China, in 2007 and 2009, respectively, and the Ph.D. degree in environmental studies from Tohoku University, Sendai, Japan, in 2013.

From April 2013 to March 2014, he was with the Center for Northeast Asian Studies, Tohoku University, as a Research Fellow. He is currently an Assistant Professor with the Institute of Electromagnetics and Acoustics, Xiamen University, Xiamen, China. His current research interests include development of ground-penetrating radar systems and algorithms for a wide variety of applications, such as nondestructive testing in civil engineering, environmental monitoring, archeological investigation, and lunar exploration.

Dr. Liu received the Young Researcher Award of the 14th International Conference on Ground Penetrating Radar in 2012 and the Excellent Paper Award of the IET International Radar Conference in 2013.

Guangyou Fang received the B.S. degree in electrical engineering from Hunan University, Changsha, China, in 1984, and the M.S. and Ph.D. degrees in electrical engineering from Xi'an Jiaotong University, Xi'an, China, in 1990 and 1996, respectively.

From 1990 to 1999, he was an Engineer, Associate Professor, and Professor with China Research Institute of Radio wave Propagation. From 2000 to 2001, he was a Visiting Scholar with the University of Trieste and International Center for Science and High Technology, Italy. From 2001 to 2003, he was a special foreign Research Fellow of the Japan Society for Promotion of Science, working with the Professor Motoyuki Sato with Tohoku University, Japan. He was the PI of CE-3 lunar penetrating radar. Since 2004, he has been a Professor with the Institute of Electronics of Chinese Academy of Sciences (IECAS), the Director of the Key Lab of Electromagnetic Radiation and Sensing Technology of CAS, and the Deputy Director of IECAS from 2013. He has published more than 300 papers in refereed journals and conference proceedings. His research interests include electromagnetic field theory, ultrawideband radar, ground-penetrating radar, lunar and mars exploration radar, geophysical electromagnetic exploration technology, and THz Imaging.

Feng Han received the B.S. degree in electronic science from Beijing Normal University, Beijing, China, in 2003, the M.S. degree in geophysics from Peking University, Beijing, in 2006, and the Ph.D. degree in electrical engineering from Duke University, Durham, NC, USA, in 2011.

He is currently an Assistant Professor with the Institute of Electromagnetics and Acoustics, Xiamen University, Xiamen, China. His research interests include ionosphere remote sensing by radio atmospherics, electromagnetic full-wave inversion by integral equations, subsurface imaging, and the design of an electromagnetic detection system.

Qing Huo Liu (S'88–M'89–SM'94–F'05) received the B.S. and M.S. degrees in physics from Xiamen University, Xiamen, China, in 1983 and 1986, respectively, and the Ph.D. degree in electrical engineering from the University of Illinois at Urbana-Champaign, Champaign, IL, USA, in 1989.

From September 1986 to December 1988, he was with the Electromagnetics Laboratory, University of Illinois at Urbana-Champaign, as a Research Assistant, and from January 1989 to February 1990, as a Postdoctoral Research Associate. From 1990 to 1995, he was a Research Scientist and Program Leader with Schlumberger-Doll Research, Ridgefield, CT, USA. From 1996 to May 1999, he was an Associate Professor with New Mexico State University. Since June 1999, he has been with Duke University, Durham, NC, USA, where he is currently a Professor in the Department of Electrical and Computer Engineering. He has published more than 400 papers in refereed journals and 500 papers in conference proceedings. His research interests include computational electromagnetics and acoustics, inverse problems, and their applications in nanophotonics, geophysics, biomedical imaging, and electronic packaging.

Dr. Liu is a Fellow of the Acoustical Society of America, a Fellow of the Electromagnetics Academy, and a Fellow of the Optical Society of America. He currently serves as the Deputy Editor in Chief of the *Progress in Electromagnetics Research*, an Associate Editor for the IEEE TRANSACTIONS ON GEOSCIENCE AND REMOTE SENSING, and an Editor of the *Journal of Computational Acoustics*. He also served as the Guest Editor for the PROCEEDINGS OF THE IEEE. Since August 2015, he has been serving as the Founding Editor-in-Chief of the new IEEE JOURNAL ON MULTISCALE AND MULTIPHYSICS COMPUTATIONAL TECHNIQUES. He serves as an IEEE Antennas and Propagation Society Distinguished Lecturer for 2014–2016. He received the 1996 Presidential Early Career Award for Scientists and Engineers from the White House, the 1996 Early Career Research Award from the Environmental Protection Agency, and the 1997 CAREER Award from the National Science Foundation. He received the 2017 ACES Technical Achievement Award.